



OPEN

Extremely hard and tough high entropy nitride ceramics

Dmitry Moskovskikh¹, Stepan Vorotilo¹, Veronika Buinevich¹, Alexey Sedegov¹, Kirill Kuskov¹, Alexander Khort², Christopher Shuck³, Maksim Zhukovskiy⁴ & Alexander Mukasyan⁵

Simultaneously hard and tough nitride ceramics open new venues for a variety of advanced applications. To produce such materials, attention is focused on the development of high-entropy ceramics, containing four or more metallic components distributed homogeneously in the metallic sublattice. While the fabrication of bulk high-entropy carbides and borides is well established, high-entropy nitrides have only been produced as thin films. Herein, we report on a novel three-step process to fabricate bulk high-entropy nitrides. The high-entropy nitride phase was obtained by exothermic combustion of mechanically-activated nanostructured metallic precursors in nitrogen and consolidated by spark plasma sintering. The fabricated bulk high-entropy nitride ($\text{Hf}_{0.2}\text{Nb}_{0.2}\text{Ta}_{0.2}\text{Ti}_{0.2}\text{Zr}_{0.2}\text{N}$) demonstrates outstanding hardness (up to 33 GPa) and fracture toughness (up to $5.2 \text{ MPa}\cdot\text{m}^{1/2}$), significantly surpassing expected values from mixture rules, as well as all other reported binary and high-entropy ceramics and can be used for super-hard coatings, structural materials, optics, and others. The obtained results illustrate the scalable method to produce bulk high-entropy nitrides with the new benchmark properties.

High-entropy (HE) ceramics are solid solutions based on interstitial phases (carbides, borides, silicides, etc.) and contain 4 or more metallic species, which endow them with unique physical and mechanical properties as a result of entropy stabilization^{1–3}. HE ceramics have attracted increasing interest, as they surpass binary ceramics (such as TiC, TiN, SiC, Si_3N_4 , ZrO_2 , Al_2O_3) in terms of hardness, fracture toughness, corrosion resistance, and high-temperature stability^{4–6}. Among conventional ceramics, transition-metal nitrides (TMN) have historically been used as cutting tools and wear-resistant coatings because of their high hardness and strength, high melting points, excellent thermal conductivity, coupled with thermal and chemical stability^{7–10}. The hardness and toughness of TMN and related solid solutions with FCC structure are interrelated functions of electron valence. As the valence electron concentration (VEC) is minimized, the hardness is maximized (usually at $\text{VEC} = 8.4$); oppositely, when the valence is maximized, the toughness is minimized (at $\text{VEC} \geq 10$)^{7,11,12} as the result of antibonding state occupation-induced lattice softening^{13,14}. For example, in $\delta\text{-TiN}_{1-x}$ the microhardness maximum occurs at $\delta\text{-TiN}_{0.67}$, which corresponds to 7.3 valence electrons¹⁴. An increased valence electron concentration resulting from higher nitrogen content leads to a decrease in hardness. This is the reason why zirconium and titanium carbonitrides have lower hardness when carbon atoms are replaced with nitrogen¹⁵. However, for $\delta\text{-HfN}_{1-x}$ a smooth increase in microhardness with nitrogen content is observed, due to the difference in 5f electron bonding states¹⁵. Thus, hardness and fracture toughness are inversely related in nitride ceramics, and bypassing this effect would lead to extraordinary properties and more widespread use.

Ternary nitride (TN) systems are predicted to be supertough—harder and more ductile than binary systems—due to the increased valence electron concentration^{12,16,17}. Various research groups have studied the effect of valence electron concentration on mechanical properties for the design of advanced TMNs¹⁷. According to Balasubramanian et al.¹² the optimized hardness and toughness in TMNs are expected at VEC of 9.0–9.5. A brittle-to-ductile transition is expected at a critical $\text{VEC} = 10$ and a transition to mechanical instability at $\text{VEC} = 10.6$. However, the calculated phonon dispersion curves indicate a dynamical stability-to-instability transition between $\text{VEC} = 9$ and 10, which is smaller than the critical $\text{VEC} = 10.6$ for the mechanical stability-instability transition. Overall, a narrow region between $\text{VEC} = 9$ and 10 is outlined for the search of phases with the highest toughness. Considering this, $\text{Ti}_{0.5}\text{Ta}_{0.5}\text{N}$ ($\text{VEC} = 9.5$) possesses one of the highest among TNs theoretical and experimentally

¹National University of Science and Technology MISiS, Moscow 119049, Russia. ²KTH Royal Institute of Technology, 114 28 Stockholm, Sweden. ³A.J. Drexel Nanomaterials Institute and Department of Materials Science and Engineering, Drexel University, Philadelphia, PA 19104, USA. ⁴Notre Dame Integrated Imaging Facility, University of Notre Dame, Notre Dame, IN 46556, USA. ⁵Department of Chemical and Biomolecular Engineering, University of Notre Dame, Notre Dame, IN 46556, USA. ✉email: mos@misis.ru; khort@kth.se

measured hardness values up to 31 GPa^{17,18}. We believe, this result can be further expanded upon by engineering high-entropy nitrides (HEN).

To date, HENs are predominantly produced as thin films^{19–25}, due to their enhanced solubility and phase stability²⁶ compared to bulk ceramics. Jin et al.²⁷ reported the synthesis of powdered metal HEN $V_{0.2}Cr_{0.2}Nb_{0.2}Mo_{0.2}Zr_{0.2}N_{1-x}$ by planetary ball milling a mixture of five transition-metal chlorides with urea and subsequent annealing of the reactive mixture under N_2 flow. The resulting powders were tested as supercapacitors, but neither the sintering nor mechanical testing was reported. Therefore, the goal of our work was the development of fabrication technology and studying the structure, and mechanical properties of a bulk HEN ceramic ($Hf_{0.2}Nb_{0.2}Ta_{0.2}Ti_{0.2}Zr_{0.2}N$).

The fabricated composition was based on the ternary $Ti_{0.5}Ta_{0.5}N$ ceramic with the highest reported hardness^{17,18,28,29}. Three additional metallic constituents were added to produce the entropy stabilization effect³. The additional metals were chosen to retain VEC close to 9.5. The article shows the results of the successful application of the complex technology of CS-SPS consolidation of mechanically activated powders for bulk HEN ceramics production and can be used for mass production of high-quality bulk HE ceramics of different types.

Results and discussion

The convex hulls for the Hf–Nb–Ta–Ti–Zr–N system were constructed at various chemical nitrogen potentials (μ_N) to estimate the range where all constituent metals could form mono-nitrides (Supplementary Table S-I in Supplementary Information). The decrease of μ_N corresponds to an increase in temperature or decrease of nitrogen partial pressure in the system. The stability range of mono-nitrides decreases in the following order: TiN (space group Fm3m, stable at $-7.952 < \mu_N < -11.249$), ZrN (space group Fm3m, stable at $-8.584 < \mu_N < -11.399$), HfN (space group Fm3m, stable at $-9.501 < \mu_N < -11.463$), TaN (space group P62m, stable at $-9.033 < \mu_N < -10.98$), NbN (space group P6m2, stable at $-8.778 < \mu_N < -9.98$). The μ_N range in which all five mono-nitrides coexist is limited to $-9.033 < \mu_N < -9.98$. This limited stability range complicates the synthesis of bulk HENs and accounts for the lack of published reports on this topic.

The MaterialsProject database contains the data on multiple TNs: $Zr_{0.5}Ti_{0.5}N$, $Hf_{0.5}Zr_{0.5}N$, $Ta_{0.5}Nb_{0.5}N$, $Ta_{0.5}Ti_{0.5}N$, $Zr_{0.5}Nb_{0.5}N$, $Ti_{0.5}Nb_{0.5}N$, $Hf_{0.5}Ti_{0.5}N$, $TaTi_2N_3$, etc. Among them, only one TN phase $Hf_{0.5}Zr_{0.5}N$ (space group R3m) was found to be stable in the investigated system (stability range $-9.333 < \mu_N < -11.492$). Although its energy of formation from HfN and ZrN is relatively low (-5 kJ/mol at $0^\circ C$), the relatively broad stability range increases the probability of formation of $Hf_{0.5}Zr_{0.5}N$ as an intermediate phase during the employed three-step processing. This finding is consistent with the predictions of Sun et al.³⁰, who indicated HfZrN as the only stable TN in the TM1–TM2–N systems (TM = Ta, Hf, Ti, Zr, Nb, V).

Most of the binary nitrides in TM1–TM2–N systems (TM = Ti, Zr, Hf, Ta, Nb, V) are predicted to be thermodynamically unstable yet meta-stabilizable³⁰. In a narrow μ_N interval of $-9.333 < \mu_N < -9.033$, the $Hf_{0.5}Zr_{0.5}N$ phase undergoes decomposition while all 5 mono-nitrides retain stability (Supplementary Table S-I). The co-existence of mono-nitride phases might be instrumental for the formation of a HEN solid solution.

The first preparation stage allowed us to make composite particles involving all five metals mixed on sub-micron sized layers of metallic constituents (Fig. 1a,g). Due to the cold-welding phenomenon during milling, thin layers of metals with a thickness of 10–100 nm formed in the bulk of each particle, providing high homogeneity for their mixing. The EDS analysis indicated that the ratio between the metals remained to be equimolar. Also, milling at relatively low speed (200 rpm) and under high pressure of pure argon allowed to produce powders with low concentrations of impurities. The XRD patterns (Fig. 1d) of thus prepared powders showed that all metals retained their crystallinity even after 10 h of mechanical treatment.

The goal of the second preparation stage is to introduce nitrogen into the system in the form of metal nitrides, as well as nitrogen solid solutions. This task was accomplished by using energy-saving combustion synthesis method³¹. Supplementary Table S-II demonstrates that the reactions between considered metals and nitrogen are highly exothermic with adiabatic combustion temperature well above 3000 K. The reaction between the metal composite particles and nitrogen was initiated locally by hot tungsten wire, followed by the rapid combustion front propagation along with the media. The total nitridation process duration was ~ 5 s. It can be seen that the combustion of such reactive metal particles in a nitrogen atmosphere leads to the formation of multiple nitride phases (Fig. 1b,e), among which there was detected the predicted $Hf_{0.5}Zr_{0.5}N_{1-x}$ TN phase. The microstructure of the inner part of the composite particles became coarser (Fig. 1b) with the grain size in the range 0.5–1 μm . A mixed hafnium-zirconium-based oxide phase was also present in the combustion products (Fig. 1h), which presumably originated due to the oxygen impurities in the initial powders and exposure of mechanically activated mixture to air during the pressing of green pellets for combustion synthesis.

In the third stage, the SPS of the synthesized complex metal nitride particles were used to produce bulk ceramics. After the SPS at the experimentally optimized conditions, the measured relative density of the ceramics was 96.6% of the theoretical maximum. The obtained HEN phase is characterized by narrow grain size distribution (10–16 μm) and crystals of polyhedral, mostly hexagonal, shape (Fig. 1c). Moreover, the $Hf_{0.5}Zr_{0.5}N_{1-x}$ TN phase was not found in the sintered specimens (Fig. 1f,i), indicating its successful conversion into the HEN. The lattice constant $a = 0.4443$ was calculated based on the XRD pattern of the HEN (Fig. 1f). According to the results of XRD and EDS analysis ~ 4.2 mol% of the (Hf,Zr) O_x phase, formed during the combustion synthesis, retained in the sintered ceramics (Fig. 1f,i). The amount of oxides is relatively small and, we suppose, could be removed by applying additional technological steps or by adjusting the technological process.

Detailed TEM investigations (Fig. 2) were performed to confirm the presence of a HEN in the sintered specimens and to define the composition of the HEN phase. HRTEM (Fig. 2a) and selected area diffraction pattern (SAED) (Fig. 2b) confirm the single-phase structure of sintered high entropy nitride. The indexed SAED pattern revealed the FCC structure of HEN with the d-spacing values $d_{020} = 0.221$ nm, $d_{200} = 0.221$ nm, $d_{220} = 0.157$ nm,

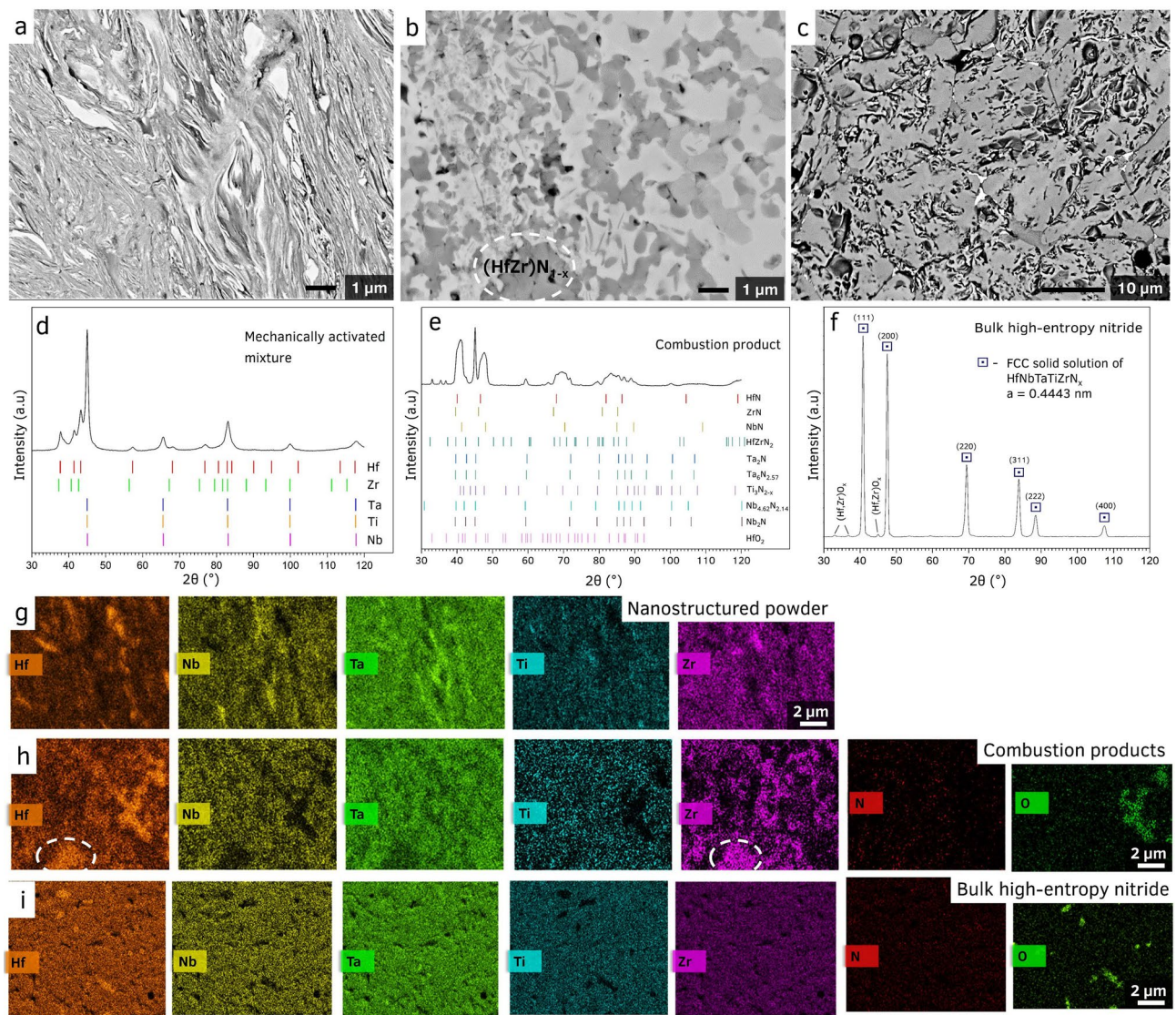


Figure 1. SEM cross-sections of (a) mechanically activated mixture Hf + Nb + Ta + Ti + Zr, (b) combustion products, (c) and spark plasma sintered high-entropy nitride. Corresponding XRD patterns of the (d) mechanically activated mixture Hf + Nb + Ta + Ti + Zr mixture, (e) after combustion synthesis, and (f) after spark plasma sintering. The EDS maps for the (g) mechanically activated mixture show that the phases have close contact, but are still separated, (h) combustion products showing multiple distinct elemental distributions, and (i) showing the fully compact, homogeneous HEN.

and $d_{240} = 0.099$ nm. The value of SAED-derived lattice constant $a = 0.443 \pm 0.001$ nm is in excellent agreement with the value calculated from XRD data. Advanced EDS mapping (Fig. 2c) demonstrates the uniform distributions of all elements along with the HEN phase. The EDS analysis of different selected areas (Supplementary Table S-III) showed the following statistically proven composition of the phase in at. %: N (28.9 ± 3.2); Hf (11.0 ± 0.4), Zr (11.0 ± 0.8); Ti (15.1 ± 0.5); Nb (15.8 ± 0.8) and Ta (18.0 ± 0.9). The lower amount of Hf and Zr in comparison with other metals could be explained by the formation of crystals of separate (Hf,Zr)O_x phase during the CS step and its recrystallization and consolidation during the SPS (Fig. 1f and Supplementary Fig. S1).

The hardness and Vickers fracture toughness of this high entropy nitride were measured at 4.9–98 N loads and compared to mono-nitrides and nitride solid solutions reported in the literature (Supplementary Table S-IV). The measured hardness $HV_{0.5}$ and elastic modulus of HEN are 32.8 ± 1.6 GPa and 352 ± 17 GPa, respectively. The elastic modulus value is comparable with the value of 360 GPa, obtained in coatings³². An increase in the indentation load leads to a gradual decrease of the hardness to $HV_{10} = 22.5 \pm 1.4$ GPa (Fig. 3). However, the experimentally measured values of hardness and fracture toughness of the HEN ceramic surpasses the values calculated based on the rule of the mixture on 130% and 82%, respectively ($HV_1 = 31.2 \pm 3.6$ GPa and $K_{IC} = 5.2 \pm 0.18$ MPa are the experimental data, and $m^{1/2}$ ROM $HV_1 = 13.6$ GPa, $K_{IC} = 2.85$ MPa·m^{1/2} are the calculated). It should be noticed, the measured results for our HEN are significantly higher the previously reported values for carbide, nitride, and silicide ceramics, including the HE compositions (Fig. 3). Moreover, the hardness values of

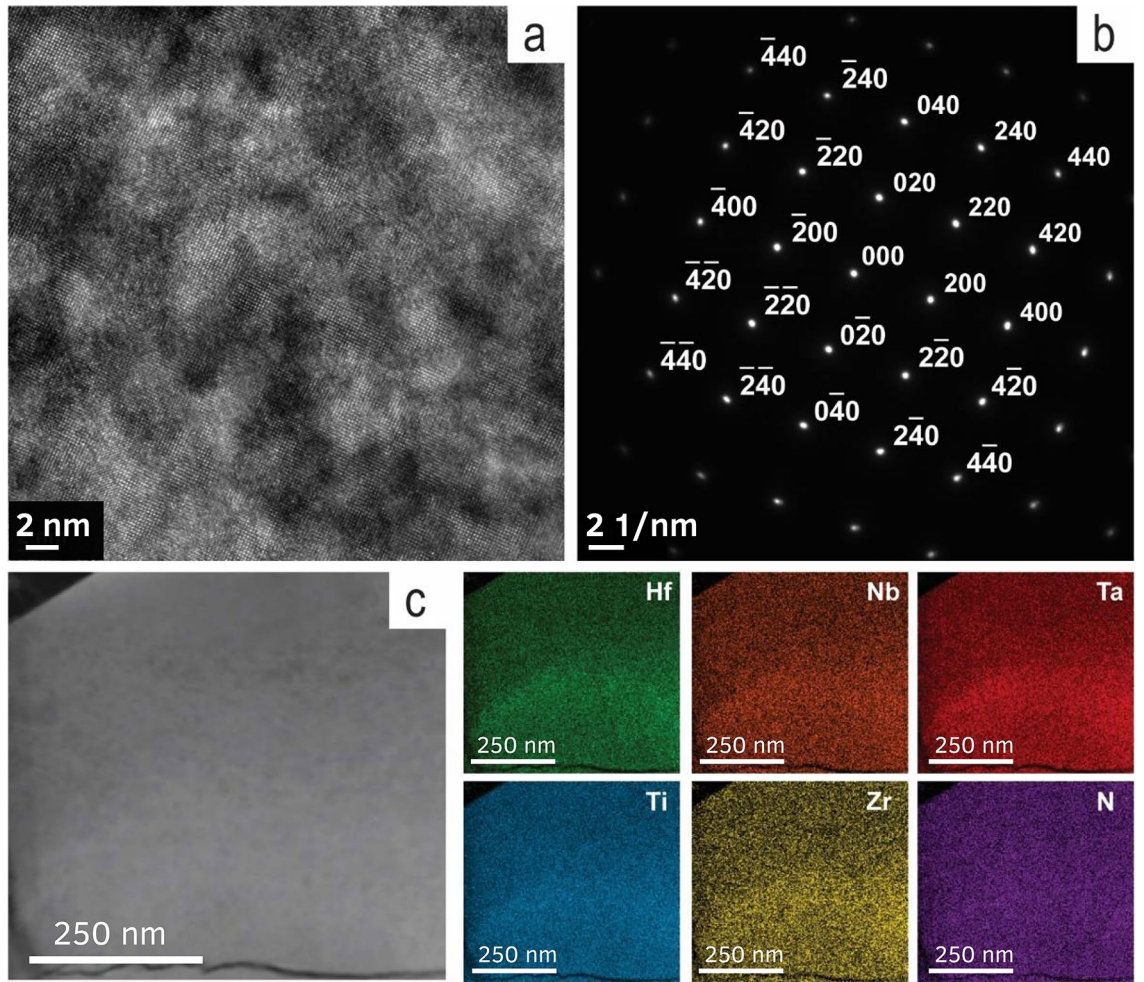


Figure 2. (a) HRTEM image of spark plasma sintered high-entropy nitride; (b) selected area electron diffraction of $(\text{HfNbTaTiZr})\text{N}_x$ taken along the $[001]$ zone axis; (c) EDS elemental mapping of the $(\text{HfNbTaTiZr})\text{N}_x$ phase.

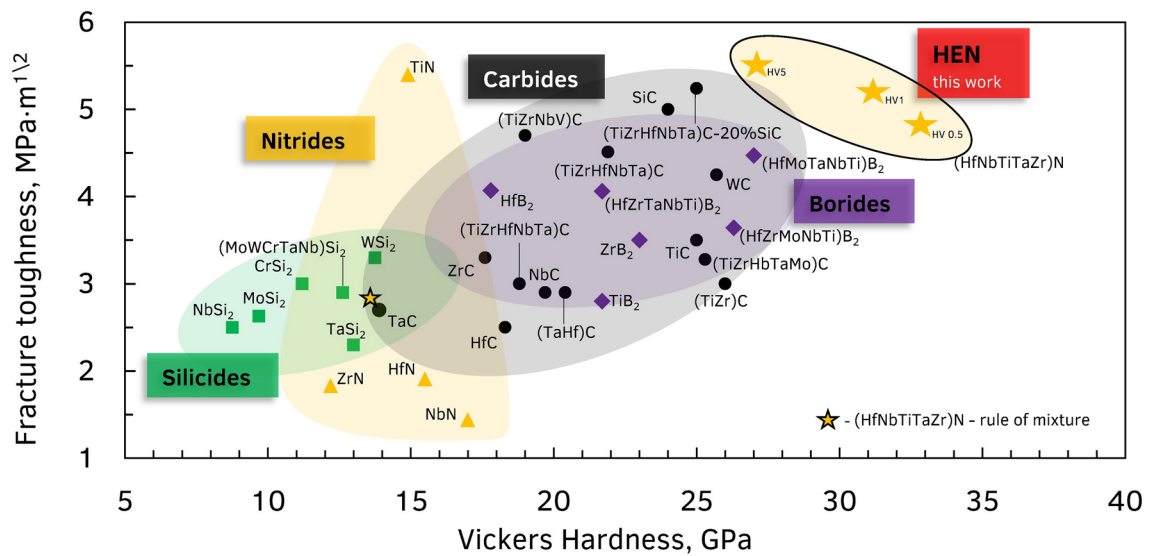


Figure 3. Fracture toughness versus hardness plot with measured values for high-entropy nitride and previously reported ceramics.

HfN ($\text{Hf}_{0.2}\text{Nb}_{0.2}\text{Ta}_{0.2}\text{Ti}_{0.2}\text{Zr}_{0.2}\text{N}$) far surpassed the estimations for both TNs phases $\text{Ti}_{0.5}\text{Nb}_{0.5}\text{N}$ (17.3 GPa) and $\text{Ti}_{0.5}\text{Ta}_{0.5}\text{N}$ (17.5 GPa) by Sangiovanni¹⁷. The breakdown of the values provided in Fig. 3 can be found in Supplementary Information (Supplementary Table S-IV).

Earlier, Sarker et al.³ described an explicit strengthening effect in HE carbides. The hardness of sintered $\text{Hf}_{0.2}\text{Nb}_{0.2}\text{Ta}_{0.2}\text{Ti}_{0.2}\text{Zr}_{0.2}\text{C}$ ceramic of 32 GPa is 40% above the value calculated by the rule of mixture (23 GPa). A similar entropy-induced strengthening effect might be responsible for the increased hardness of the HfN, obtained in this work. Previously, enhancement of the mechanical performance of TMN was achieved by engineering alternating layers of TMNs and more ductile body-centered cubic metals³³. Similarly, nanocomposite structures developed by Voevodin and Zabinski³⁴ demonstrates high hardness at stresses below the elastic strength limit, while at extreme loading their mechanical behavior switches to ductile, thus preventing brittle failure. A related effect might be responsible for the increase of the fracture hardness of the HfNs due to possible nanoscale precipitates of ductile elements (i.e. Ta) on the boundaries of HfN grains during the sintering.

Moreover, as the valence electron concentration of the HfNs is close to the optimal value of 9.5, derived by Guo³⁵ and Sangiovanni¹⁷, the “lattice softening” effect could also contribute to the increased fracture toughness of the HfN phase. The effect of a simultaneous considerable increase of hardness and fracture toughness in HfN warrants closer investigation and theoretical modeling. However, these results indicate that HfNs have the potential to become the new benchmark ceramic for structural and machining applications since the mechanical performance of the (HfNbTaTiZr)N ceramic developed in this work is considerably superior to conventional SiC, TiC, TiN, and TiB₂.

Conclusions

1. Grand potential phase diagram modeling revealed that mono-nitrides of Hf, Zr, Ta, Nb, and Ti are stable at relatively narrow nitrogen potential range $-9.033 < \mu_{\text{N}} < -9.98$ and that trigonal $\text{Hf}_{0.5}\text{Zr}_{0.5}\text{N}$ is the only stable at $-9.333 < \mu_{\text{N}} < -11.492$ TN in the system. A nitrogen potential range was indicated ($-9.033 < \mu_{\text{N}} < -9.333$) where this trigonal phase will decompose into FCC ZrN and HfN to facilitate the formation of FCC HfN solid solution.
2. Based on the proposed model, a three-stage synthesis protocol was developed to produce bulk HfN ceramics, including mechanical treatment of the metallic constituents in an argon atmosphere, combustion of mechanically-induced nanostructured particles in nitrogen, and spark plasma sintering of the combustion products.
3. The bulk ceramics are primarily composed of hexagonal grains (10–15 μm) of the HfN phase. The sintered HfN ($\text{Hf}_{0.2}\text{Nb}_{0.2}\text{Ta}_{0.2}\text{Ti}_{0.2}\text{Zr}_{0.2}\text{N}$) demonstrates outstanding hardness (up to 33 GPa) and fracture toughness (5.2 $\text{MPa}\cdot\text{m}^{1/2}$), which is significantly higher in comparison with theoretical estimations and carbide, nitride, and silicide ceramics, including TNs and other HfEs.
4. The strengthening effect presumably results from entropy stabilization and optimization of valence electron concentration of the HfN phase. The obtained ceramic is a promising candidate for practical application in multiply areas, where special mechanical properties are required.
5. A scalable approach for the fabrication of bulk HfN by the complex CS-SPS consolidation of mechanically activated powders, is proposed for the first time. While the only one HfN system was studied here, countless possible other HfNs can be produced using the developed technological approach.

Methods

Calculation of grand potential phase equilibria. To analyze the phase equilibria in this system, the formation enthalpies for nitride phases were calculated using mixed GGA and GGA + U (semiempirically-tuned generalized gradient approximations) frameworks, which is known for its ability to correctly predict the phase stability³⁶. Grand potential phase diagrams at varied nitrogen potentials were calculated using PDApp software, which is integrated into Materials API^{37,38} and employs a database of DFT computed bulk material energies with crystal structures obtained from the Inorganic Crystal Structure Database (ICSD)³⁹ and those generated by applying data-mined chemical substitutions^{40,41}.

Fabrication of high-entropy ceramics. Figure 4 provides the schematic for the three-stage process employed for the synthesis of bulk high-entropy nitride ceramics. The overall processing method includes three stages: (i) preparation of the reactive nanocomposite powders by high energy ball milling (HEBM); (ii) combustion synthesis (CS) of TNs; and (iii) spark plasma sintering (SPS) of the bulk HfN ceramics.

Preparation of reactive composite powders. The metallic powders of Hf, Nb, Ta, Ti and Zr (RusRed-Met, Russia, > 99% purity) with a particle size distribution of 40–60 μm were used for preparation of a precursor mixtures. HEBM of reactive mixtures was conducted in an argon atmosphere (4 atm, 99.998%) using a double-station planetary ball mill (Activator-2s, Russia) equipped with steel mill and steel grinding medium (balls). Batches consisted of 20 g powders and were mixed in an equimolar ratio Hf:Nb:Ta:Ti:Zr = 1:1:1:1:1 using 250 ml steel jars and 6 mm steel balls. The ball to powder mixture weight ratio was 20:1. The milling speed was 200 rpm at a rotational coefficient of K = 1. The total duration of the mechanical treatment was 10 h. The goal is to produce nanostructured composite particles, which involve all five components.

Combustion synthesis. Mechanically induced nanostructured composite Hf/Nb/Ta/Ni/Zr particles were placed in a laboratory chemical reactor. Initially, the reactor was vacuumed and then filled with gaseous nitrogen

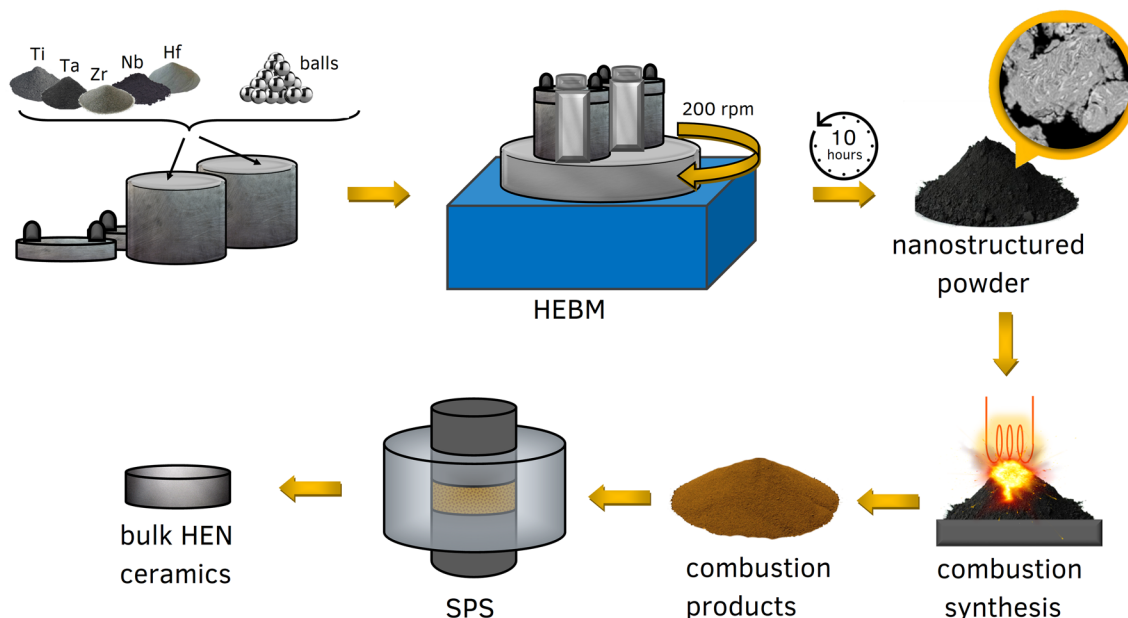


Figure 4. Schematic showing the fabrication process. Initially, the metal powders are HEBM in a planetary ball mill for 10 h. This mixture then undergoes CS under a nitrogen atmosphere. Finally, the powders are transferred to an SPS device, where they undergo the final stage of reaction/consolidation in a nitrogen atmosphere.

up to 8 atm. Powder mixtures were locally preheated using a hot tungsten wire to initiate a chemical reaction with the subsequent propagation of a self-sustaining combustion front. At this stage, the metal nitrides were synthesized. The combustion products were then ball-milled for 2 h at 60 rpm using WiseMixSBML mill (DAIHAN Scientific, South Korea) equipped with 250 ml steel jars and 6 mm steel balls. The ball to powder mixture weight ratio was 6:1.

Spark Plasma Sintering of bulk ceramics. The synthesized powders were consolidated in an SPS system (Labox 650, SinterLand, Japan) in a nitrogen atmosphere (0.8 atm) at 2073 K. The dwell time was 20 min at a pressure of 30 MPa, the heating rate was 100 °C/min. Bulk ceramic samples in the form of disks with a diameter of 20 mm and a thickness of 5–6 mm were produced by SPS.

Material characterization. X-ray diffraction (XRD) was applied for the study of phase composition of the fabricated materials using DRON-4-07 (Russia) monochromatic Co-K α radiation. The structure of the experimental materials was analyzed via scanning electron microscopy (SEM) on a Vega 3 (TESCAN, Czech Republic) and JSM-7600F (JEOL, Japan) with a microanalysis system (EDX, Oxford Instruments) and a high-resolution transmission electron microscopy (TEM) on TITAN 800-300 (Thermo Fisher Scientific, USA) equipped with an Ultim Max EDS system (Oxford Instruments).

Vickers hardness tests were used for the study of the microhardness of the synthesized materials [Emco-Test DuraScan 70 (Austria)]. The applied loads varied from 0.5 to 10 N. The fracture toughness was measured using the Vickers indentation-induced cracks corresponding to the Anstis method⁴². The elastic modulus was measured by Anton Paar CSM Micro Indentation Tester (Austria) under applied loads of 100 mN.

Received: 25 July 2020; Accepted: 3 November 2020

Published online: 16 November 2020

References

- Bérardan, D., Franger, S., Dragoe, D., Meena, A. K. & Dragoe, N. Colossal dielectric constant in high entropy oxides. *Phys. Status Solidi Rapid Res. Lett.* **10**, 328–333 (2016).
- Harrington, T. J. *et al.* Phase stability and mechanical properties of novel high entropy transition metal carbides. *Acta Mater.* **166**, 271–280 (2019).
- Sarker, P. *et al.* High-entropy high-hardness metal carbides discovered by entropy descriptors. *Nat. Commun.* **9**, 4980 (2018).
- Zhang, Y. *et al.* Microstructures and properties of high-entropy alloys. *Prog. Mater. Sci.* **61**, 1–93 (2014).
- Chang, X., Zeng, M., Liu, K. & Fu, L. Phase engineering of high-entropy alloys. *Adv. Mater.* **32**, 1907226 (2020).
- Oses, C., Toher, C. & Curtarolo, S. High-entropy ceramics. *Nat. Rev. Mater.* **5**, 295–309 (2020).
- Jhi, S.-H., Ihm, J., Louie, S. G. & Cohen, M. L. Electronic mechanism of hardness enhancement in transition-metal carbonitrides. *Nature* **399**, 132–134 (1999).
- Aouadi, S. M. Structural and mechanical properties of TaZrN films: Experimental and ab initio studies. *J. Appl. Phys.* **99**, 053507 (2006).
- Kim, D.-J. *et al.* Properties of TiN–TiC multilayer coatings using plasma-assisted chemical vapor deposition. *Surf. Coat. Technol.* **116–119**, 906–910 (1999).

10. Maerky, C., Guillou, M.-O., Henshall, J. L. & Hooper, R. M. Indentation hardness and fracture toughness in single crystal TiC0.96. *Mater. Sci. Eng. A* **209**, 329–336 (1996).
11. Richter, V., Beger, A., Drobniowski, J., Endler, I. & Wolf, E. Characterisation and wear behaviour of TiN- and TiCxN1-x-coated cermets. *Mater. Sci. Eng. A* **209**, 353–357 (1996).
12. Balasubramanian, K., Khare, S. V. & Gall, D. Valence electron concentration as an indicator for mechanical properties in rocksalt structure nitrides, carbides and carbonitrides. *Acta Mater.* **152**, 175–185 (2018).
13. Lengauer, W. & Ettmayer, P. Lattice parameters and thermal expansion of δ -VN_{1-x} from 298–1000 K. *Monatshfte fuer Chemie/ Chemical Mon.* **117**, 713–719 (1986).
14. Lengauer, W. Nitrides: Transition metal solid-state chemistry. In *Encyclopedia of Inorganic and Bioinorganic Chemistry* 1–24 (Wiley, Hoboken, 2015). <https://doi.org/10.1002/9781119951438.eibc0146.pub2>.
15. Yang, Q., Lengauer, W., Koch, T., Scheerer, M. & Smid, I. Hardness and elastic properties of Ti(C₂N_{1-x}), Zr(C₂N_{1-x}) and Hf(C₂N_{1-x}). *J. Alloys Compd.* **309**, L5–L9 (2000).
16. Sangiovanni, D. G., Chirita, V. & Hultman, L. Electronic mechanism for toughness enhancement in Ti_xM_{1-x}N (M = Mo and W). *Phys. Rev. B* **81**, 104107 (2010).
17. Sangiovanni, D. G., Hultman, L. & Chirita, V. Supertoughening in B1 transition metal nitride alloys by increased valence electron concentration. *Acta Mater.* **59**, 2121–2134 (2011).
18. Wiemer, C., Sanjinés, R. & Lévy, F. Deposition and characterization of refractory ternary phases: The transition metal nitride Ti_{1-x}Mo_xN_y. *Surf. Coat. Technol.* **86–87**, 372–376 (1996).
19. Chang, S.-Y. *et al.* Improved diffusion-resistant ability of multicomponent nitrides: From unitary TiN to senary high-entropy (TiTaCrZrAlRu)N. *JOM* **65**, 1790–1796 (2013).
20. Liu, L., Zhu, J. B., Hou, C., Li, J. C. & Jiang, Q. Dense and smooth amorphous films of multicomponent FeCoNiCuVZrAl high-entropy alloy deposited by direct current magnetron sputtering. *Mater. Des.* **46**, 675–679 (2013).
21. Yan, X. H., Li, J. S., Zhang, W. R. & Zhang, Y. A brief review of high-entropy films. *Mater. Chem. Phys.* **210**, 12–19 (2018).
22. Sobol, O. V. *et al.* Reproducibility of the single-phase structural state of the multielement high-entropy Ti–V–Zr–Nb–Hf system and related superhard nitrides formed by the vacuum-arc method. *Tech. Phys. Lett.* **38**, 616–619 (2012).
23. Pogrebnyak, A. D. *et al.* Influence of residual pressure and ion implantation on the structure, elemental composition, and properties of (TiZrAlYNb)N nitrides. *Tech. Phys.* **60**, 1176–1183 (2015).
24. Zhang, Y., Yan, X.-H., Liao, W.-B. & Zhao, K. Effects of nitrogen content on the structure and mechanical properties of (Al_{0.5}CrFeNiTi_{0.25})N_x high-entropy films by reactive sputtering. *Entropy* **20**, 624 (2018).
25. Sheng, W., Yang, X., Wang, C. & Zhang, Y. Nano-crystallization of high-entropy amorphous NbTiAlSiW_xN_y films prepared by magnetron sputtering. *Entropy* **18**, 226 (2016).
26. Matenoglou, G. M. *et al.* Structure, stability and bonding of ternary transition metal nitrides. *Surf. Coat. Technol.* **204**, 911–914 (2009).
27. Jin, T. *et al.* Mechanochemical-assisted synthesis of high-entropy metal nitride via a soft urea strategy. *Adv. Mater.* **30**, 1707512 (2018).
28. Abadias, G. *et al.* Reactive magnetron cosputtering of hard and conductive ternary nitride thin films: Ti–Zr–N and Ti–Ta–N. *J. Vac. Sci. Technol. A Vac. Surf. Film.* **28**, 541–551 (2010).
29. Weast, R. C. Handbook of chemistry and physics, 49th ed. *Am. J. Med. Sci.* **257**, 423 (1969).
30. Sun, W. *et al.* A map of the inorganic ternary metal nitrides. *Nat. Mater.* **18**, 732–739 (2019).
31. Mukasyan, A. S. *et al.* The solid flame phenomenon: A novel perspective. *Adv. Eng. Mater.* <https://doi.org/10.1002/adem.201701065> (2018).
32. Pogrebnyak, A. D. *et al.* The effect of the deposition parameters of nitrides of high-entropy alloys (TiZrHfVNB)N on their structure, composition, mechanical and tribological properties. *J. Superhard Mater.* **35**, 356–368 (2013).
33. Madan, A. *et al.* Enhanced mechanical hardness in epitaxial nonisostructural Mo/NbN and W/NbN superlattices. *J. Appl. Phys.* **84**, 776–785 (1998).
34. Voevodin, A. & Zabinski, J. Supertough wear-resistant coatings with ‘chameleon’ surface adaptation. *Thin Solid Films* **370**, 223–231 (2000).
35. Guo, X. *et al.* Hardness of covalent compounds: Roles of metallic component and d valence electrons. *J. Appl. Phys.* **104**, 023503 (2008).
36. Jain, A. *et al.* Formation enthalpies by mixing GGA and GGA + U calculations. *Phys. Rev. B* **84**, 045115 (2011).
37. Ong, S. P., Wang, L., Kang, B. & Ceder, G. Li–Fe–P–O₂ Phase diagram from first principles calculations. *Chem. Mater.* **20**, 1798–1807 (2008).
38. Ong, S. P., Jain, A., Hautier, G., Kang, B. & Ceder, G. Thermal stabilities of delithiated olivine MPO₄ (M = Fe, Mn) cathodes investigated using first principles calculations. *Electrochem. Commun.* **12**, 427–430 (2010).
39. Belsky, A., Hellenbrandt, M., Karen, V. L. & Luksch, P. New developments in the Inorganic Crystal Structure Database (ICSD): Accessibility in support of materials research and design. *Acta Crystallogr. Sect. B Struct. Sci.* **58**, 364–369 (2002).
40. Ong, S. P. *et al.* The Materials Application Programming Interface (API): A simple, flexible and efficient API for materials data based on REpresentational State Transfer (REST) principles. *Comput. Mater. Sci.* **97**, 209–215 (2015).
41. Lu, Z. & Ciucci, F. Metal borohydrides as electrolytes for solid-state Li, Na, Mg, and Ca batteries: A first-principles study. *Chem. Mater.* **29**, 9308–9319 (2017).
42. Anstis, G. R., Chantikul, P., Lawn, B. R. & Marshall, D. B. A critical evaluation of indentation techniques for measuring fracture toughness: I, direct crack measurements. *J. Am. Ceram. Soc.* **64**, 533–538 (1981).

Acknowledgements

This work was conducted with the financial support of the Russian Science Foundation (Grant no. 18-79-10215). SV expresses special gratitude to Anna Ceban for her support and help in work and life.

Author contributions

D.M. conceived the idea and designed the experiments. V.B. and A.S. conducted the experiments. D.M. and S.V. collected all data and images presented in the paper. K.K. conducted the SEM and M.Z. conducted the HRTEM. S.V. conducted the hardness measurements. S.V. and D.M. wrote the initial version of this paper; D.M., S.V., K.K., A.K., C.S. and A.M. revised the manuscript critically. All authors analyzed the data and discussed the results. D.M. supervised this study.

Funding

Open Access funding provided by Kungliga Tekniska Hogskolan.

Competing interests

The authors declare no competing interests.

Additional information

Supplementary information is available for this paper at <https://doi.org/10.1038/s41598-020-76945-y>.

Correspondence and requests for materials should be addressed to D.M. or A.K.

Reprints and permissions information is available at www.nature.com/reprints.

Publisher's note Springer Nature remains neutral with regard to jurisdictional claims in published maps and institutional affiliations.



Open Access This article is licensed under a Creative Commons Attribution 4.0 International License, which permits use, sharing, adaptation, distribution and reproduction in any medium or format, as long as you give appropriate credit to the original author(s) and the source, provide a link to the Creative Commons licence, and indicate if changes were made. The images or other third party material in this article are included in the article's Creative Commons licence, unless indicated otherwise in a credit line to the material. If material is not included in the article's Creative Commons licence and your intended use is not permitted by statutory regulation or exceeds the permitted use, you will need to obtain permission directly from the copyright holder. To view a copy of this licence, visit <http://creativecommons.org/licenses/by/4.0/>.

© The Author(s) 2020